iScience

CellPress
OPEN ACCESS

Article

Terahertz multi-level nonvolatile optically rewritable encryption memory based on chalcogenide phase-change materials

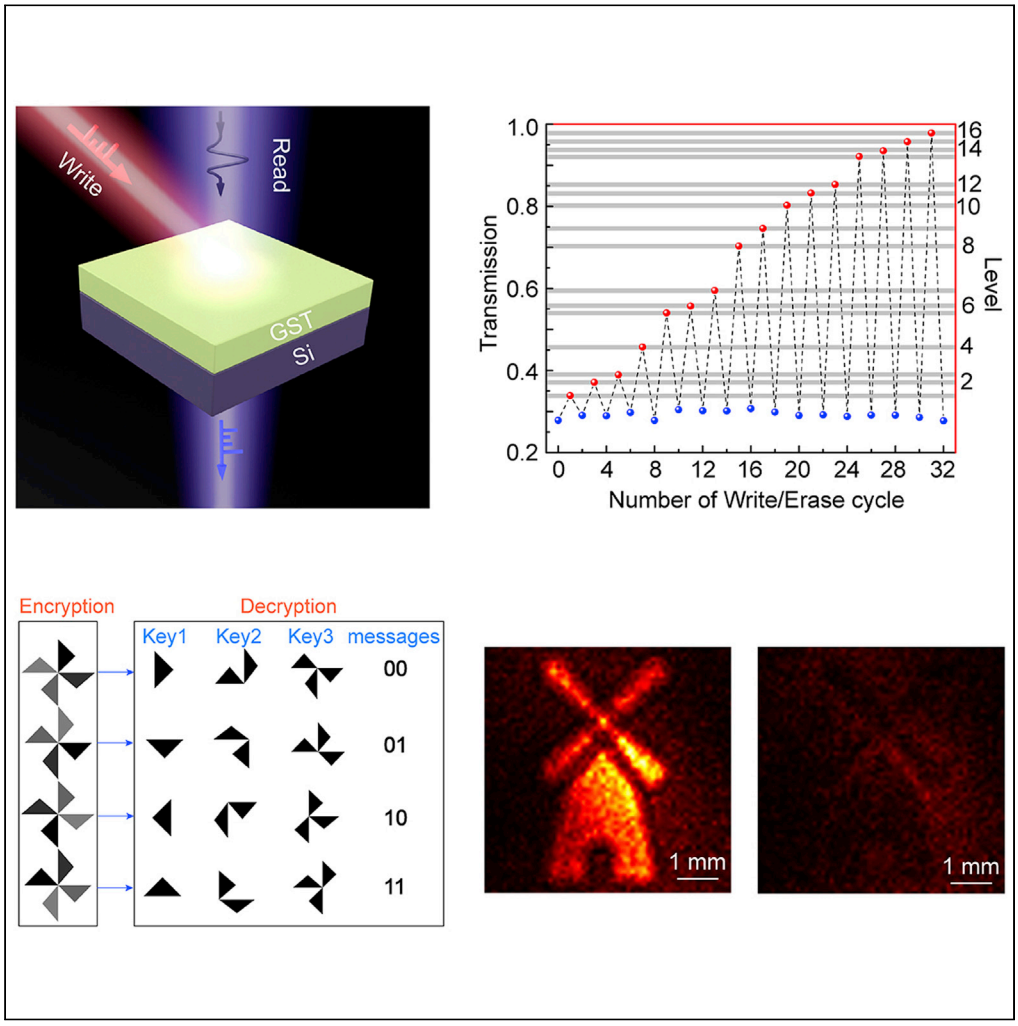

Shoujun Zhang, Xieyu Chen, Kuan Liu, ..., Jianming Dai, Tun Cao, Zhen Tian

jianmingdai@tju.edu.cn (J.D.)
caotun1806@dlut.edu.cn (T.C.)
tianzhen@tju.edu.cn (Z.T.)

Highlights

Multiple intermediate states and large-area amorphization of GST in the THz regime

4-ns operating speed, excellent reproducibility, and long-term stability

Multiple writing-erasing tests on hexadecimal coding information memories

THz photoprint memory and encryption memory

Zhang et al., iScience 25, 104866
August 19, 2022
https://doi.org/10.1016/j.isci.2022.104866

iScience

CellPress
OPEN ACCESS

Article

Terahertz multi-level nonvolatile optically rewritable encryption memory based on chalcogenide phase-change materials

Shoujun Zhang,[1] Xieyu Chen,[1] Kuan Liu,[2] Haiyang Li,[2] Yuanhao Lang,[1] Jie Han,[1] Qingwei Wang,[1] Yongchang Lu,[1] Jianming Dai,[1,*] Tun Cao,[2,*] and Zhen Tian[1,3,4,*]

SUMMARY

Fast and efficient information processing and encryption, including writing, reading, and encryption memory, is essential for upcoming terahertz (THz) communications and information encryption. Here, we demonstrate a THz multi-level, nonvolatile, optically rewritable memory and encryption memory based on chalcogenide phase-change materials, $Ge_2Sb_2Te_5$ (GST). By tuning the laser fluence irradiated on GST, we experimentally achieve multiple intermediate states and large-area amorphization with a diameter of centimeter-level in the THz regime. Our memory unit features a high operating speed of up to 4 ns, excellent reproducibility, and long-term stability. Utilizing this approach, hexadecimal coding information memories are implemented, and multiple writing-erasing tests are successfully carried out in the same active area. Finally, terahertz photoprint memory is demonstrated, verifying the feasibility of lithography-free devices. The demonstration suggests a practical way to protect and store information and paves a new avenue toward nonvolatile active THz devices.

INTRODUCTION

Wireless data traffic has increased exponentially in recent years owing to the rapid development of mobile terminals and the Internet of Things (Cherry, 2004). Such a remarkable growth in network capacity has driven the urge to investigate much higher wireless transmission rates (Kürner and Priebe, 2014). The realization of an ultra-high communication rate requires the support of ultra-broad working bandwidth. To this end, the THz band (0.1-10 THz), which promises broad bandwidth ranging from tens of GHz to several THz, has attracted widespread attention (Kleine-Ostmann and Nagatsuma, 2011; Tonouchi, 2007). And as such, THz communications is crucial to the development of upcoming sixth-generation (6G) mobile communication networks (Song and Nagatsuma, 2011), and can be applied to long-distance, medium-distance, indoor and near-field communications (Nagatsuma et al., 2016). Promising applications of THz communications include wireless backhaul (Boulogeorgos et al., 2018; Narytnyk and Engineering, 2014), wireless communications in data centers (Mamun et al., 2018; Peng and Kürner, 2015), information security (Ma et al., 2018), virtual reality (Chaccour et al., 2020; Hu et al., 2020; Khorsandmanesh and Emadi, 2020), device-to-device (D2D) communications (Amer et al., 2020a, 2020b; Guan et al., 2019; Mendrzik et al., 2018; Petrov et al., 2019; Yang et al., 2019), on-chip/inter-chip wireless communications (Chen and Han, 2018; Jornet and Akyildiz, 2013; Yang et al., 2016), and so forth. Therefore, THz technologies have bright application prospects in the next generation of computing and communications systems (Koenig et al., 2013; Meijer et al., 2016; Yang et al., 2020). The capability to write, store and read information is the very core part of information processing. To achieve these goals, we need high-density, rewritable THz memory devices to achieve high-speed and long-term storage of THz information. Previous research works on such THz memory devices are mainly based on indium oxide nanoparticles (Ji et al., 2019; Liu et al., 2019), perovskite structure (Xiong et al., 2020), and vanadium dioxide (Chen et al., 2020; Driscoll et al., 2009), and so forth. However, most of these methods require rigorous working environments while their achieved storage density is relatively low, making them far from meeting the demand (Chen et al., 2020; Driscoll et al., 2009; Ji et al., 2019; Liu et al., 2019; Xiong et al., 2020). In addition, in THz communications and memory devices, information encryption is extremely important, while existing THz communications and memory devices lack information protection or encryption. Traditional optical information encryption methods utilize the manipulation of wavelength (Singh et al., 2018), phase (Bao et al., 2018), polarization (Heydari et al., 2017), and orbital

[1]Center for Terahertz Waves and College of Precision Instrument and Optoelectronics Engineering, Key Laboratory of Optoelectronic Information Technology (Ministry of Education of China), Tianjin University, Tianjin 300072, China

[2]School of Optoelectronic Engineering and Instrumentation Science, Dalian University of Technology, Dalian 116024, China

[3]Georgia Tech Shenzhen Institute (GTSI), Tianjin University, Shen Zhen, 518067, China

[4]Lead contact

*Correspondence: jianmingdai@tju.edu.cn (J.D.), caotun1806@dlut.edu.cn (T.C.), tianzhen@tju.edu.cn (Z.T.)

https://doi.org/10.1016/j.isci.2022.104866

angular momentum (Fang et al., 2020), and so forth. It is hence of great significance to innovate more effective information encryption and storage methods.

Chalcogenide phase-change materials (PCMs) behave in striking contrast between amorphous and crystalline phases of optical properties (Kolobov et al., 2004; Wuttig and Yamada, 2007). And by continuously changing the crystallization fraction, we can obtain multiple intermediate phases that can be kept stable for a long time under the working environment with high reproducibility (Lin et al., 2013; Sevison et al., 2020; Sun et al., 2017; Wuttig et al., 2017). Compared with those traditional phase-change materials (VO_2), the chalcogenide PCMs offer a nonvolatile tuning mechanism, in which no additional energy is needed to maintain the functional state of the device. In particular, $Ge_2Sb_2Te_5$ (GST), as one of the most popular alloys, has led to various photonic applications, such as photonic memory (Cheng et al., 2018; Rios et al., 2014; Ríos et al., 2015), optoelectronic color display (Hosseini et al., 2014), modulators (Wang et al., 2016), switches (Gholipour et al., 2013), absorbers (Tittl et al., 2015), and thermal emitters (Du et al., 2017; Qu et al., 2017), and so forth. However, these applications are limited to the visible and infrared spectral range, leaving the extensive potential for further exploration in the THz band (Makino et al., 2019; Pitchappa et al., 2019), especially for computing, communications, information storage, and encryption.

Here, we implement PCMs GST in a THz multi-level, nonvolatile, optically rewritable memory device and propose a new method of information encryption memory. By using a nanosecond laser with tunable fluence, we experimentally investigate the amorphization characteristics of GST and realize multi-level modulation of THz signals. X-ray diffraction (XRD) measurements show that the mechanism of modulation is the continuous varying of crystallinity fraction. Subsequently, we encode the THz data in hexadecimal and achieve multi-level, multi-bit storage, in marked contrast to the previous research. High-speed writing rate at nanosecond level, high reproducibility, and long-term stability has been experimentally achieved. As a proof-of-concept, we successfully performed multiple writing-erasing tests in the same area of the study. Finally, to improve the storage density, we carry out the writing-erasing process of photographic data read by a near-field scanning terahertz microscopy system. Our new approach extends the application of GST to the THz band, providing new ideas for information memory, modern cryptography, and security applications, with specific achievements on a nanosecond, large-scale, multi-level amorphization of GST. Furthermore, this work will empower the development of more nonvolatile THz functional devices.

RESULTS

A terahertz memory and encryption cell

Figure 1A shows the schematic and operating principle of our THz multi-level, nonvolatile, optically rewritable memory device. An 80-nm-thick GST thin film is deposited on a 1-mm-thick silicon (Si) substrate. By controlling the intensity and pulse width of control pulses, the phase state of the GST memory element is changed, resulting in the change in THz transmission owing to the different conductivities in amorphous (A-GST) and crystalline (C-GST) states. C-GST exhibits higher conductivity and thus lower THz transmission than A-GST. Therefore, such GST memory states are programmable and the stored information can be readout with THz waves. As illustrated in Figure 1B, totally different bonding structures between A-GST and C-GST lead to striking optical contrasts in the two states. Previous studies (Huang and Robertson, 2010; Kooi and Wuttig, 2020; Shportko et al., 2008; Wuttig et al., 2018; Zhu et al., 2018) have shown that A-GST has typical covalent bonds, whereas C-GST has metavalent bonds and the atomic arrangement of A-GST is more random than that of C-GST. In general, the amorphous-to-crystalline transition is an annealing process and can be achieved by applying long and relatively moderate pulses (optical or electrical) to locally heat A-GST to its crystallization temperature T_c or by heating the whole cell up (i.e. thermal) and holding for a short time. This way, the stored information can be erased. By contrast, amorphization can be achieved by applying high-intensity pulses with a short duration to heat the C-GST above the melting point T_m and then rapidly quenching it to prevent any recrystallization, and thereby, the writing operation is achieved. More importantly, unlike other phase-change materials such as VO_2, the property of GST is stable after the external stimulus is removed.

In our approach, the crystalline-to-amorphous transition of GST memory element is induced by nanosecond laser pulses with 1064-nm wavelength, 7-ns pulse width, and beam diameter of 1 cm, as shown in Figure 1A. THz time-domain spectroscopy (THz-TDS) is used to characterize the transmission response of the memory device. By tuning the average power of laser pulses, different degrees of amorphization of GST are achieved, thereby realizing information storage, named writing channel. And then the information

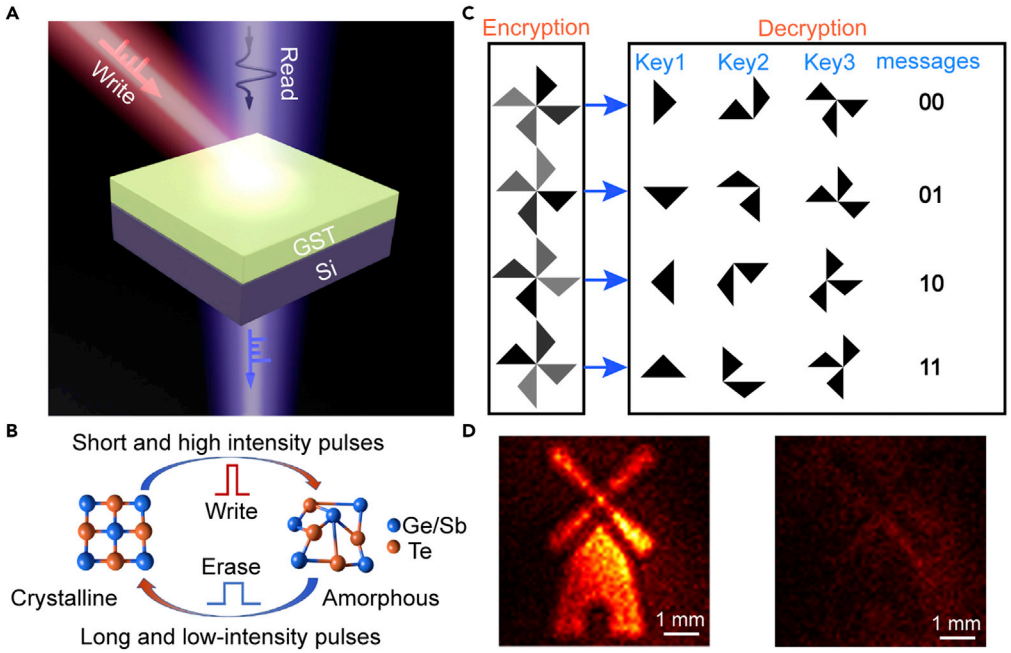

Figure 1. Operation principle of a GST-based optical multi-level encryption memory cell

(A) Control pulses with various powers are used to switch the GST from crystalline to intermediate and amorphous states, as a write channel. Information is stored in the phase states of GST, which exhibit varied THz transmission. The incident THz waves are encoded in hexadecimal, as a read channel (A-F).

(B) By applying short and high-intensity pulses, GST can be transited from crystalline to amorphous state, whereas, by using long and low-intensity pulses, GST can be switched back. Totally different bonding structures between A-GST and C-GST lead to striking optical contrasts in the two states.

(C) Demonstration of optical encryption memory. The information is encrypted and stored in a sixteen-level grayscale windmill pattern. Different binary patterns can be observed by using different thresholds (i.e., keys), and distinct messages can be obtained by referring to the corresponding codebook. Various data can be accessed by rotating the windmill under the same key.

(D) Demonstration of high-density information storage: Take the writing and erasing of a windmill pattern as an example.

encoding and reading process are tested by THz waves, which exhibit different transmission under different GST phase states, named reading channel. The stored data can be erased by recrystallizing GST, as mentioned above, the local area of GST can be erased by optical or electrical pulses. Whereas, in our experiment, we heat the entire GST memory element to 300°C and maintain it for 2 min to erase the whole stored information, so that a large amount of information can be repeatedly erased and written in the same area. Another reason for using the heating process rather than the short laser pulse irradiation process is explained as follows: Amorphous GST transforms into a hexagonal closed packed phase (HCP) when it is heated up to around 300°C while it is transferred into a face-centered cubic phase (FCC) when the sample is irradiated by short laser pulses (Chiang et al., 1999; Lu et al., 2013); the THz wave transmission change through the sample during the amorphous-to-HCP process is more dramatic, in comparison to the case during the amorphous-to-FCC process (Makino et al., 2019). In addition to information memory, to further realize the encrypted memory of information, we propose a novel information encryption design that is substantially different from traditional encryption methods, as shown in Figure 1C. A windmill composed of four basic geometric patterns with different in-plane locations serves as a storage unit. The sender encrypts the information and stores it in a sixteen-level gray-scale windmill map, which corresponds to our sixteen-level storage. Different information (00,01,10,11) can be encrypted by rotating the windmill. Each fan blade of the windmill has a different gray level, and the receiver converts it to binary notation. Different thresholds (keys) can be used to obtain diverse fan blade combinations. The information represented by different patterns can be accessed by consulting the codebook. For example, the first windmill pattern in Figure 1C can be decoded with keys 1, 2, and three to obtain information 00, 11, and 10, respectively. To get the correct information, the stealer first has to know that our information is stored in binary, and then to find the correct keys and the corresponding cipher book. And the change in the keys

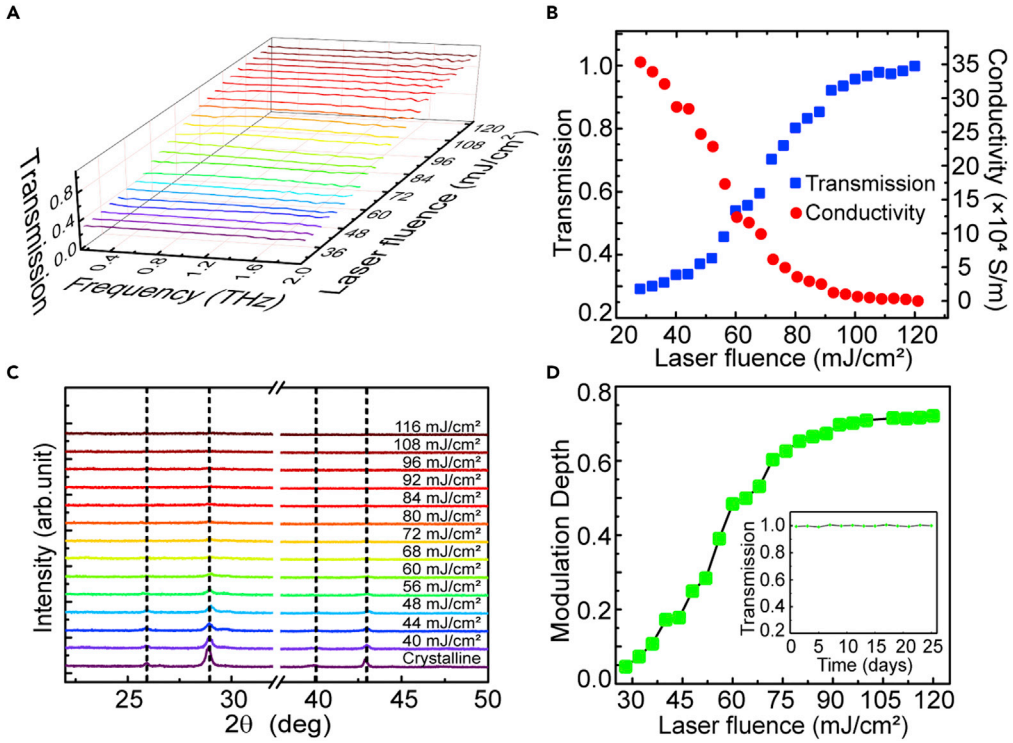

Figure 2. Phase transitions characterization of GST

(A) Broadband THz transmission of GST under laser irradiation with different fluences.

(B) Extracted transmission at one THz from (A) and corresponding calculated conductivity.

(C) Measured XRD patterns of GST under laser irradiation with different fluences.

(D) The modulation depth of the memory cell at one THz under irradiation of a single laser pulse with various fluences from 28 mJ/cm^2 to 120 mJ/cm^2. The inset in (D) shows the data retention capability of the memory device over many days.

can be realized by dynamically changing the gray level of the windmill, which will greatly improve the security of messages. To further improve the information memory density and realize the information encryption, we propose and experimentally characterize the high-density information memory, as shown in Figure 1D. The writing and erasing of windmill patterns have been realized (see Figure 5 for details). Our design is energy-efficient and simple and consequently can lead to novel THz data encryption memory with long-term stability.

Amorphization characterization of the device

First, we investigate the THz transmission of the GST memory element by applying a laser pulse train with single-pulse energy fluence varying from 28 mJ/cm^2 to 120 mJ/cm^2 in an incremental step of 4 mJ/cm^2 to the sample, as shown in Figure 2A. When the laser pulse is incident on the device, the GST film absorbs the pulse energy and generates heat. As the incident laser pulse energy is getting high enough, the device temperature is increased over that of the amorphization. After the laser pulse passes by it cools quickly owing to the short pulse width, and as a result, GST undergoes a crystalline-to-amorphous phase change. We find that the THz transmission through the sample gradually increases with increasing laser fluence and the transmission curves are flat across the entire THz spectrum. It is noteworthy that, large GST amorphization size/area has been achieved, with an area reaching a diameter of approximately 1 cm, and the result lays the foundation for the development of more active THz devices. Based on this achievement, one can expect to synthesize large-size broadband THz modulators using GST.

In order to better illustrate the dependence of the transmission on irradiation laser fluence, transmittances at one THz when the sample is pumped at different laser fluences are selected, as shown in Figure 2B. We can see that the transmission increases slowly at the beginning until the pump fluence reaches 44 mJ/cm^2. And then, a linear response appears as the laser fluence is tuned beyond the switching threshold, followed

by a saturation regime, indicating almost all of HCP has been transformed into A-GST. Mathematically, the real part of THz conductivity of GST σ can be extracted using the film transmission formula (Li et al., 2015):

$$|\tilde{t}(\omega)| = \frac{1+n_{si}}{1+n_{si}+Z_0\sigma d} \quad \text{(Equation 1)}$$

where Z_0 = 377 Ω is the wave impedance of vacuum, n_{si} = 3.42 is the refraction index of silicon substrate, and d = 80 nm is the thickness of GST film. As shown in Figure 2B, the conductivity decreases with the increasing laser fluence. The blue and red dots in Figure 2B show THz transmission and conductivity, respectively. Experimental results shown in Figure 2B indicate that the conductivity of the sample changes from ~350000 S/m to nearly 0 as the pump laser fluence is increased from 0 to 116 mJ/cm^2, resulting in the corresponding change in THz wave transmission from ~30% to nearly 100%.

The principle of multi-level storage in the GST memory device is further investigated by X-ray diffraction (XRD) measurements at different laser fluences, as shown in Figure 2C. Each sample is irradiated by a single pulse with a pulse width of 7 ns and pump laser fluence varying from 0 to 116 mJ/cm^2. In Figure 2C, we set breaks to remove those intense peaks diffracted from silicon substrates. It can be seen that, without laser irradiation, the diffraction pattern of the crystalline GST shows very pronounced peaks at ~26°, ~29°, ~40°, and ~43°, which correspond to the $(10\bar{2})$, $(10\bar{3})$, $(10\bar{6})$ and $(2\bar{1}0)$ lattice planes of the HCP GST, respectively. As the irradiation fluence continuously increases all the diffraction peaks started to decrease until they completely disappeared when the pump laser fluence reaches over 108 mJ/cm^2, indicating that the entire HCP GST sample has been transformed into A-GST. Results from the above dynamic XRD measurements with varied laser fluence also imply that there are mixed states consisting of both crystalline and amorphous regions and that, with the increase of laser fluence, the relative amount of HCP decreases, and hence the volume fraction of the amorphous state has increased. The transition of these mixed states lies between those of HCP GST and A-GST, as discussed above.

In Figures 2A–2C, it can be seen that our device can achieve multi-level modulation. In order to further illustrate the modulation characteristics of the memory device, we calculated the modulation depth (MD), which represents the change in THz transmission under different fluences (see Figure 2D). The following equation is used for the calculation:

$$MD = \frac{T_{p_i} - T_{cry}}{T_{p_i}} \quad \text{(Equation 2)}$$

where T_{p_i} and T_{cry} are THz transmittances when the writing fluence is p_i and 0 mJ/cm^2, respectively. When a pump laser fluence of ~44 mJ/cm^2 is applied, an 18% modulation depth can be achieved. As the fluence increases to ~108 mJ/cm^2, the modulation depth reaches a saturation point at ~72%.

Terahertz memory performance

As discussed above, multi-level memory can be achieved by varying laser fluence. In order to achieve more storage levels and appropriate contrasts between neighboring levels, we select those fluence values in the linear regime in Figure 2B. The THz time-domain signals transmitted through the device under different laser fluences are shown in Figure 3A. As the fluence is increased, the THz signal strength increases while the entire THz waveform experiences a left shift, which suggests that the complex index of refraction is reduced. Our multi-level storage operation is illustrated in Figure 3B. Using optical pulses with different laser fluences ranging from 44 mJ/cm^2 to 108 mJ/cm^2, which are selected from Figure 2B, we can achieve 16 distinguishable levels. It should be noted that, in order to demonstrate the multi-level storage capability, we only select those energy values with large contrast between adjacent levels from Figure 2B, and in fact, more levels can be achieved by simply using smaller energy intervals. Information can be stored in our memory device in hexadecimal encoding, and meanwhile, be erased at any level by setting GST back to the crystalline state. 16 levels are clearly distinct (levels "0" to "F") and each level can be achieved by precisely setting a single-pulse fluence. Therefore, we can achieve 16-level storage in a single memory unit, which greatly improves storage density compared with existing THz storage methods (Chen et al., 2020; Driscoll et al., 2009; Ji et al., 2019; Liu et al., 2019; Xiong et al., 2020), and our writing-erasing procedures are simple and effective. In addition, sixteen-level storage is helpful for us to realize the encrypted memory device, as proposed in Figure 1D.

High writing speed is required for THz communications and modulation devices. To further characterize the storage performance of our device, writing time measurements of the GST memory unit are carried out. A

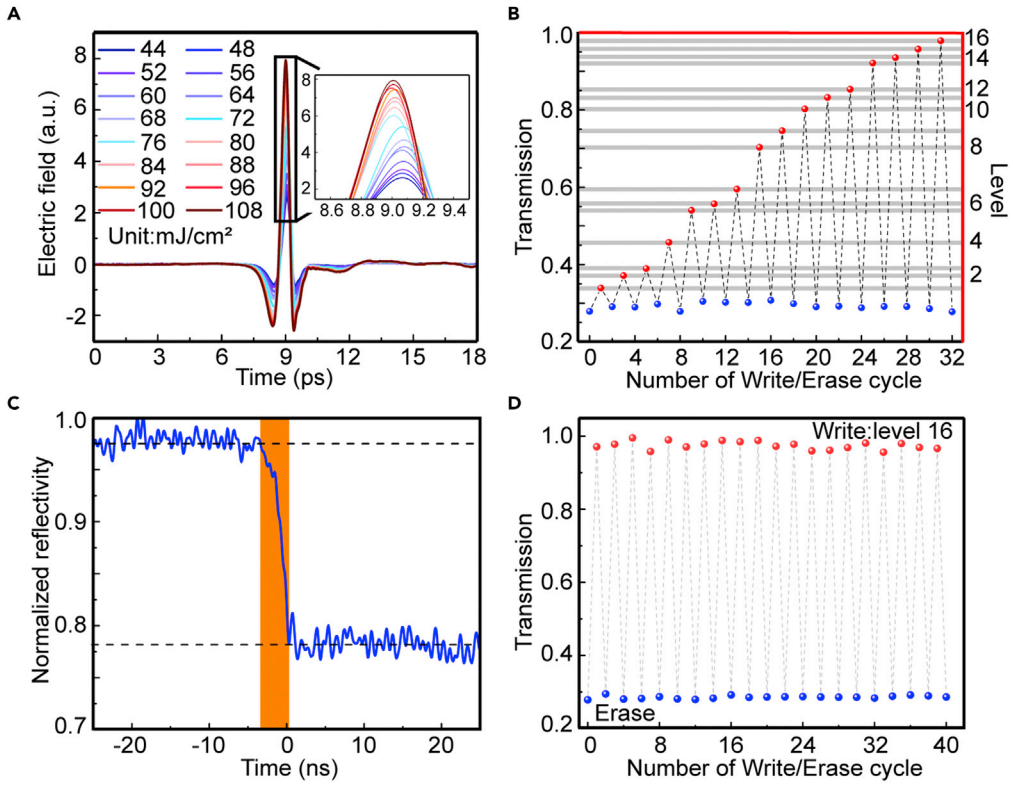

Figure 3. Memory performance of the device

(A) Measured time-domain THz signals through the memory cell at sixteen pump energies. A magnified view of the signals is shown in the inset.

(B) Sixteen storage levels and corresponding THz transmissions.

(C) The writing speed of 4 ns is measured by a pump-probe system.

(D) Repeatability of the switching between level "16" and erased status.

pump-probe system is employed for real-time reflectivity measurements. We use a nanosecond laser to irradiate (pump) the GST sample and a 532-nm continuous-wave laser to probe the change in reflectivity. In our experiment, a 108 mJ/cm^2 pump laser is used to transform HCP GST to amorphous GST and the consequent transient process is probed by a continuous wave incident on the center of the pump beam spot at an incident angle of ~45°. Using a high-speed silicon detector with a rising time of 150 ps and a fast oscilloscope with a sampling rate of five GSa/s, we are able to measure the reflected laser pulse and record the entire writing process. A 532 nm band-pass filter is placed in front of the detector to avoid other light interference. Figure 3C shows the normalized reflectivity change when a GST memory element is irradiated by a single laser pulse with an energy fluence of 108 mJ/cm^2. The reflectivity decreases from its initial high level to the final low level, which corresponds to the crystalline and amorphous phases, respectively. It can be seen from Figure 3C that the transition is completed within ~4 ns and the reflectivity change is ~20%. During this process, the melting and rapid solidification of the crystal grains occurs successively (Huang et al., 2009; Siegel et al., 2008). Experimental results shown above indicate that we achieve a writing time of 4 ns, corresponding to a writing speed/rate of ~0.25 GHz, which is significant for high-speed storage. And we realize the erasing process by heating the device on a hot plate at 300° for 2 min.

Besides writing speed, good reversibility and stability are two more important factors for memory devices. The erasing-writing cycles are carried out and the results are shown in Figure 3D. The initial state of GST (sample) is in fully crystallized phase and subsequently transformed into the amorphous phase by applying a single laser pulse with a energy fluence of 108 mJ/cm^2 and pulse width of 7 ns. Phase change switching, along with a subsequent THz transmission change of 78%, has been repeated over 20 cycles. It can be seen that the transmission does not show any deterioration during all cycles. The fluctuation in amplitude is caused by the instability of the laser fluence, measurement system, as well as small variation in the

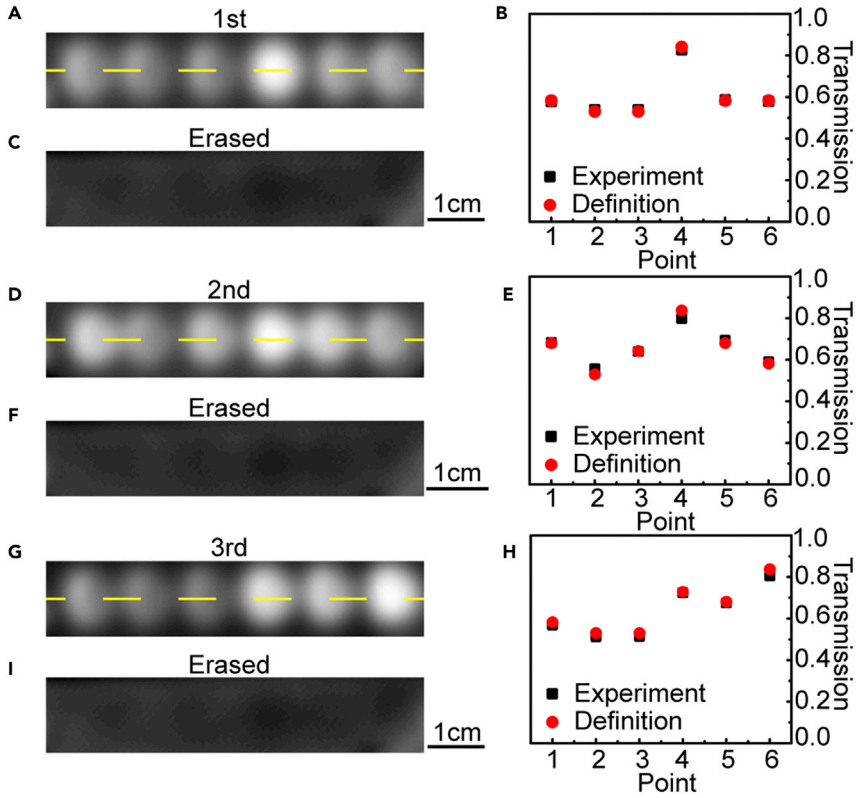

Figure 4. Rewriteable memory with hexadecimal encoding

(A-C) The writing, reading, and erasing results of "TJU."

(D-F) The writing, reading, and erasing results of "tju."

(G-I) The writing, reading, and erasing results of "THz."

(B, E, and H) Comparison of experimental and defined results. The experimental results are read based on the average transmission at the positions along the yellow dotted line in (A, D, and G).

measurement position. More cycles are feasible as the endurance characteristic of PCM cells has been proved to reach 10^{12} cycles in previous reports (Farmakidis et al., 2019; Lee et al., 2007; Pirovano et al., 2004; Raoux et al., 2014; Simpson et al., 2011), and so, the proposed memory device is suitable for storage applications. We next investigate the data retention capability of the memory device. As shown in the inset of Figure 2D, the THz amplitude transmittance can be stable for over 25 days. And the actual stable time can be much longer as it has already been reported that the GST phase states can be stable for years (Kolobov et al., 2004).

Terahertz rewritable multi-level memory

In the above section, we demonstrate that the proposed device is suitable for THz memory applications. Different laser fluences can induce different degrees of amorphization, that is, multi-level, multi-bit storage can be realized. The principle and process of rewritable multi-level storage are described as follows: we first encode the information in hexadecimal and each character is represented by two hexadecimal letters. And then each letter is written on the memory cell by applying different laser fluences on GST to achieve different degrees of amorphization. Finally, the stored data can be erased by completely crystallizing GST memory cells on a hot plate. By repeating the above steps, different information can be written and erased in the same area.

Writing-erasing tests are conducted by encoding and deleting "TJU" as "54 4A 55" in hexadecimal. Each hexadecimal character represents a single pulse with a certain laser fluence. Different degrees of amorphization are achieved by irradiating different positions with corresponding laser fluence. The encoded information is read with a fiber-laser-based THz spectroscopic imaging system. The sample is placed on a two-dimensional translation stage. The THz amplitude transmission imaging of "TJU" is shown in Figure 4A. In the image, the dark

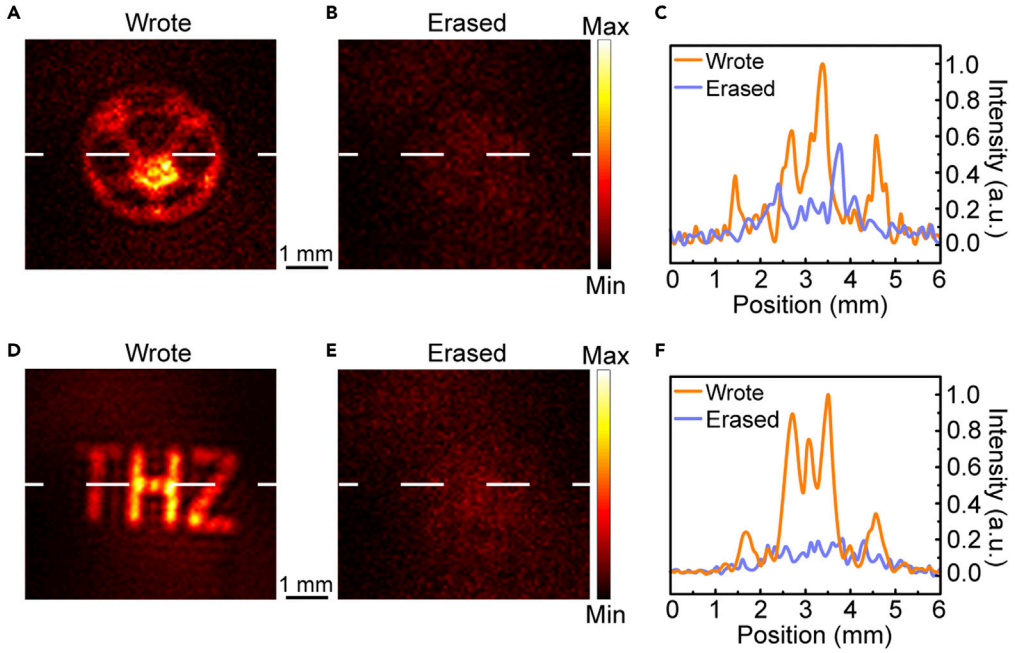

Figure 5. High-density prints memory

High-density information storage of designed memory cells has been experimentally verified by using a near-field scanning terahertz microscopy system.

(A-C) The writing and erasing results of basketball and corresponding cross-section normalized intensity values extracted from (A and B).

(D-F) The writing and erasing results of "THz" and corresponding cross-section normalized intensity values extracted from (D and E).

background corresponds to crystalline GST while the bright spots represent the encoded information. Under different laser fluences, different degrees of amorphization of GST can be achieved, and consequently the THz transmission is modulated, resulting in significant difference in brightness. Therefore, we can read the stored information based on the average transmission at the positions along the yellow dotted line in Figure 4A. As shown in Figure 4B, the black dots are the read data and the red dots are the defined transmission. As such, the information "TJU" can be read correctly. Figure 4C shows the THz image after the information is erased by heating the sample at 300 °C on a hot plate for 2 min. The stored data are erased and a new message can be re-written in the same area. Then we encode "tju" as "74 6A 75" in hexadecimal in the same area, as shown in Figure 4D, and reading results are shown in Figure 4E. Subsequently, we erase it in the same way, as shown in Figure 4F, and write another data "THz," which is encoded as "54 48 7A" into the same area. Data writing, reading, and erasing processes are carried out, and the results are shown in Figures 4G–4I. The discrepancies between the read information and the defined value are mainly caused by the laser power fluctuation. Owing to the reversibility of our GST memory device, repeatable writing-erasing cycles are feasible. The experimental results prove our design, we can achieve repeated writing, reading, and erasing of different information in the same area.

Terahertz high-density photo prints memory

In order to further improve the storage density and illustrate the memory performance of the device, the writing-erasing cycles of the photographic data are tested with a near-field scanning terahertz microscopy system. A 1064-nm nanosecond laser pulse with 108 mJ/cm^2 illuminates on a metal mask, of which images are projected onto a GST film. The illuminated regions of GST are then transformed from crystalline to amorphous states, and consequently, these illuminated regions exhibit higher transmission than those dark regions. The stored data are read by a THz near-field system and erased by thermally annealing the memory element. The writing and erasing results of a windmill (see Figure 1C), basketball, and "THZ" patterns are shown in Figure 5. The entire storage area is 6 mm by 6 mm with a minimum unit pixel size of about 0.2 mm. It can be seen from the results that the pattern information is stored in the GST memory device and the slight change in brightness of the erased region indicates the area where previous

patterns are written. Compared with the hexadecimal code storage described above, the data are directly written into the GST memory device, leading to a much higher information density. Figures 5C and 5F show the normalized intensity of the cross-section at the white dotted line in Figures 5A, 5B, 5D, and 5E. Compared with the surrounding crystallized area, the amorphized area shows higher intensity values before erasing, but similar intensity after erasing. The reason why the intensity value in some areas is still high after erasing is that the laser intensity distribution in the cross-section is not uniform and the areas irradiated with high laser intensity are damaged. With a more evenly distributed laser beam cross-section and smaller fluence, we can achieve better memory performance. Moreover, in our experiment, the pattern structure is directly written into the GST, which lays the foundation for the GST lithography-free devices. In addition, more flexible information writing can be achieved by using a spatial light modulator instead of a mask. In subsequent research, technologies such as laser direct writing can be applied to realize the encrypted memory as mentioned above.

DISCUSSION

In conclusion, we demonstrate a THz multi-level, multi-bit, nonvolatile optically rewritable memory device that exhibits large THz transmission changes induced by structural transitions in GST and presents a novel information encryption memory method. By gradually tuning the fluence of the nanosecond laser pulse, multiple intermediate states with partially amorphized GST can be formed as evidenced by XRD measurements. We encode 16 levels in hexadecimal and test writing-erasing cycles with the help of nanosecond laser pulses and thermal anneal. Both a writing speed of 4 ns and long-term stability are achieved in our memory device. In our prototype of THz GST-based memory, the writing speed, reversibility, and stability are comparable with pre-existing memory devices. Furthermore, as a proof-of-concept, we write and erase different letters in the same area of the device. Writing and reading procedures of photographic data by means of a near-field scanning terahertz microscopy system are carried out to characterize the memory performance. We believe that this is a significant report on multi-level amorphization characteristics of GST in the THz frequency range. Our work lays the foundation for a THz memory device with high writing speed, long-term stability, and good reversibility, which is significant for the next generation of high-speed computing and communications systems. In addition, the information encryption method we proposed can be applied to encryption memory in the future to improve the security of information transmission and storage. Our experiments also demonstrate the capability for high modulation depth of GST, which is essential for the realization of large-area THz active modulators, switches, and absorbers. Besides, the new approach holds great potential for application in THz integrated photonic nonvolatile devices, wearable devices, sensors, and information encryption devices. In addition, in our experiments, we verify that GST encoding can be achieved without complicated lithography procedures. Therefore, GST lithography-free devices are promising in the future.

Limitations of the study

In this work, the transition from crystalline state to amorphous state is achieved by a nanosecond laser pulse, which exhibits high writing speed. Whereas, the crystallization of GST is induced by heating the entire GST element to 300°C for 2 min, which is not enough fast compared with optical stimulus. The reason for inducing crystallization by heating instead of laser pulses is that the phase transition temperature increases with the heating rate and could exceed the melting point of GST at the ultrafast heating rate (Jeyasingh et al., 2014; Orava et al., 2012; Pries et al., 2019). The phase transition temperature from FCC to HCP induced by 7-ns laser pulse will higher than the melting point, and thus the switching from FCC to HCP is hindered, and a hot plate is adopted in our experiments. Even so, it is possible to achieve the phase transition process from FCC to HCP by some methods in the future, such as (1) by applying a laser with longer duration time. (2) decreasing the phase transition temperature of GST by doping. Besides, the present memory cannot be addressed to selectively erase the specific data, which can be realized in the future.

STAR★METHODS

Detailed methods are provided in the online version of this paper and include the following:

- KEY RESOURCES TABLE
- RESOURCE AVAILABILITY
  - Lead contact

SUPPLEMENTAL INFORMATION

Supplemental information can be found online at https://doi.org/10.1016/j.isci.2022.104866.

ACKNOWLEDGMENTS

This work was supported by the National Key Research and Development Program of China (2017YFA0701004, 2019YFA0709100, 2020YFA0714504), Tianjin Municipal Fund for Distinguished Young Scholars (Grant No. 20JCJQJC00190), and Key Fund of Shenzhen Natural Science Foundation (Grant No. JCYJ20200109150212515).

AUTHOR CONTRIBUTIONS

Z. Tian conceived the idea. S. -J. Zhang conducted the design. H. -Y. Li and K. Liu deposited the GST films. Q. -W. Wang and Y. -C. Lu helped with the sample preparation. S. -J. Zhang, X. -Y. Chen, Y. -H. Lang and J. Han performed the measurements. S. -J. Zhang wrote the article. J.-M. Dai, Z. Tian, and T. Cao revised the article and supervised the project. All authors discussed the results and commented on the article.

DECLARATION OF INTERESTS

The authors declare no competing interests.

Received: March 10, 2022
Revised: June 28, 2022
Accepted: July 27, 2022
Published: August 19, 2022

REFERENCES

Amer, R., Elsawy, H., Butt, M.M., Jorswieck, E.A., Bennis, M., and Marchetti, N. (2020a). Optimized caching and spectrum partitioning for D2D enabled cellular systems with clustered devices. IEEE Trans. Commun. *68*, 4358–4374.

Amer, R.M., ElSawy, H., Kibilda, J., Butt, M.M., and Marchetti, N. (2020b). Performance analysis and optimization of cache-assisted CoMP for clustered D2D networks. IEEE Trans. Mobile Comput. https://doi.org/10.1109/TMC.2020.3020552.

Bao, Y., Yu, Y., Xu, H., Lin, Q., Wang, Y., Li, J., Zhou, Z.K., and Wang, X.H. (2018). Coherent pixel design of metasurfaces for multidimensional optical control of multiple printing-image. Adv. Funct. Mater. *28*, 1870366.

Boulogeorgos, A.-A.A., Alexiou, A., Merkle, T., Schubert, C., Elschner, R., Katsiotis, A., Stavrianos, P., Kritharidis, D., Chartsias, P.-K., Kokkoniemi, J., et al. (2018). Terahertz technologies to deliver optical network quality of experience in wireless systems beyond 5G. IEEE Commun. Mag. *56*, 144–151.

Chaccour, C., Soorki, M.N., Saad, W., Bennis, M., and Popovski, P. (2020). Risk-based optimization of virtual reality over terahertz reconfigurable intelligent surfaces. IEEE. https://doi.org/10.1109/ICC40277.2020.9149411.

Chen, S.-C., Yuan, H.-K., Zhai, Z.-H., Du, L.-H., Zhong, S.-C., Zhu, H.-F., Shi, Q.-W., Huang, W.-X., Li, Z.-R., and Zhu, L.G. (2020). All optically driven memory device for terahertz waves. Opt. Lett. *45*, 236–239.

Chen, Y., and Han, C. (2018). Channel modeling and analysis for wireless networks-on-chip communications in the millimeter wave and terahertz bands. IEEE, 651–656. https://doi.org/10.1109/INFCOMW.2018.8406954.

Cheng, Z., Ríos, C., Youngblood, N., Wright, C.D., Pernice, W.H.P., and Bhaskaran, H. (2018). Device-level photonic memories and logic applications using phase-change materials. Adv. Mater. *30*, 1802435.

Cherry, S.J.I.s. (2004). Edholm's law of bandwidth. IEEE Spectrum *41*, 58–60.

Chiang, D., Jeng, T.-R., Huang, D.-R., Chang, Y.-Y., and Liu, C.-P. (1999). Kinetic crystallization behavior of phase-change medium. Jpn. J. Appl. Phys. *38*, 1649.

Driscoll, T., Kim, H.-T., Chae, B.-G., Kim, B.-J., Lee, Y.-W., Jokerst, N.M., Palit, S., Smith, D.R., Di Ventra, M., and Basov, D.N. (2009). Memory metamaterials. Science *325*, 1518–1521.

Du, K.-K., Li, Q., Lyu, Y.-B., Ding, J.-C., Lu, Y., Cheng, Z.-Y., and Qiu, M. (2017). Control over emissivity of zero-static-power thermal emitters based on phase-changing material GST. Light Sci. Appl. *6*, e16194.

Fang, X., Ren, H., and Gu, M.J.N.P. (2020). Orbital angular momentum holography for high-security encryption. Nat. Photon. *14*, 102–108.

Farmakidis, N., Youngblood, N., Li, X., Tan, J., Swett, J.L., Cheng, Z., Wright, C.D., Pernice, W.H.P., and Bhaskaran, H. (2019). Plasmonic nanogap enhanced phase-change devices with dual electrical-optical functionality. Sci. Adv. *5*, eaaw2687.

Gholipour, B., Zhang, J., MacDonald, K.F., Hewak, D.W., and Zheludev, N.I. (2013). An all-optical, non-volatile, bidirectional, phase-change meta-switch. Adv. Mater. *25*, 3050–3054.

Guan, K., Peng, B., He, D., Eckhardt, J.M., Rey, S., Ai, B., Zhong, Z., and Kurner, T. (2019). Measurement, simulation, and characterization of train-to-infrastructure inside-station channel at the terahertz band. IEEE Trans. Terahertz Sci. Technol. *9*, 291–306.

Heydari, E., Sperling, J.R., Neale, S.L., and Clark, A.W. (2017). Plasmonic color filters as dual-state nanopixels for high-density microimage encoding. Adv. Funct. Mater. *27*, 1701866.

Hosseini, P., Wright, C.D., and Bhaskaran, H. (2014). An optoelectronic framework enabled by low-dimensional phase-change films. Nature *511*, 206–211.

Hu, F., Deng, Y., Saad, W., Bennis, M., and Aghvami, A.H. (2020). Cellular-connected wireless virtual reality: requirements, challenges, and solutions. IEEE Commun. Mag. *58*, 105–111.

Huang, B., and Robertson, J. (2010). Bonding origin of optical contrast in phase-change memory materials. Phys. Rev. B *81*, 081204.

Huang, H., Zuo, F., Zhai, F., Wang, Y., Lai, T., Wu, Y., and Gan, F. (2009). Fast phase transition process of Ge 2 Sb 2 Te 5 film induced by picosecond laser pulses with identical fluences. J. Appl. Phys. *106*, 063501.

Jeyasingh, R., Fong, S.W., Lee, J., Li, Z., Chang, K.-W., Mantegazza, D., Asheghi, M., Goodson, K.E., and Wong, H.-S.P. (2014). Ultrafast characterization of phase-change material crystallization properties in the melt-quenched amorphous phase. Nano Lett. *14*, 3419–3426.

Ji, H., Wang, W., Xiong, L., Liu, D., Lv, L., Zhang, B., and Shen, J. (2019). Terahertz read-only multi-order nonvolatile rewritable photo-memory based on indium oxide nanoparticles. Appl. Phys. Lett. *114*, 011105.

Jornet, J.M., and Akyildiz, I.F. (2013). Graphene-based plasmonic nano-antenna for terahertz band communication in nanonetworks. IEEE J. Sel. Areas Commun. *31*, 685–694.

Khorsandmanesh, Y., and Emadi, M.J. (2020). Peak age of information analysis for virtual reality in terahertz communications. IEEE. https://doi.org/10.1109/IWCIT50667.2020.9163486.

Kleine-Ostmann, T., and Nagatsuma, T. (2011). A review on terahertz communications research. J. Infrared Millim. Terahertz Waves *32*, 143–171.

Koenig, S., Lopez-Diaz, D., Antes, J., Boes, F., Henneberger, R., Leuther, A., Tessmann, A., Schmogrow, R., Hillerkuss, D., Palmer, R., et al. (2013). Wireless sub-THz communication system with high data rate. Nat. Photon. *7*, 977–981.

Kolobov, A.V., Fons, P., Frenkel, A.I., Ankudinov, A.L., Tominaga, J., and Uruga, T. (2004). Understanding the phase-change mechanism of rewritable optical media. Nat. Mater. *3*, 703–708.

Kooi, B.J., and Wuttig, M. (2020). Chalcogenides by design: functionality through metavalent bonding and confinement. Adv. Mater. *32*, 1908302.

Kürner, T., and Priebe, S. (2014). Towards THz communications-status in research, standardization and regulation. J. Infrared Millim. Terahertz Waves *35*, 53–62.

Lee, S.-H., Jung, Y., and Agarwal, R. (2007). Highly scalable non-volatile and ultra-low-power phase-change nanowire memory. Nat. Nanotechnol. *2*, 626–630.

Li, Q., Tian, Z., Zhang, X., Singh, R., Du, L., Gu, J., Han, J., and Zhang, W. (2015). Active graphene–silicon hybrid diode for terahertz waves. Nat. Commun. *6*, 7082.

Lin, J.-C., Long, G.-Y., Wang, Y., and Wu, Y.-Q. (2013). Polarization readout analysis for multilevel phase change recording by crystallization degree modulation. Chinese Phys. B *22*, 124208.

Liu, B., Liu, J., Ji, H., Wang, W., Shen, J., and Zhang, B. (2019). Terahertz nonvolatile in situ electrically erasable-rewritable photo-memory based on indium oxide/PEDOT. Opt Express *27*, 28792–28799.

Lu, H., Thelander, E., Gerlach, J.W., Decker, U., Zhu, B., and Rauschenbach, B. (2013). Single pulse laser-induced phase transitions of PLD-deposited Ge2Sb2Te5 films. Adv. Funct. Mater. *23*, 3621–3627.

Ma, J., Shrestha, R., Adelberg, J., Yeh, C.-Y., Hossain, Z., Knightly, E., Jornet, J.M., and Mittleman, D.M. (2018). Security and eavesdropping in terahertz wireless links. Nature *563*, 89–93.

Makino, K., Kato, K., Saito, Y., Fons, P., Kolobov, A.V., Tominaga, J., Nakano, T., and Nakajima, M. (2019). Terahertz spectroscopic characterization of Ge 2 Sb 2 Te 5 phase change materials for photonics applications. J. Mater. Chem. C Mater. *7*, 8209–8215.

Mamun, S.A., Umamaheswaran, S.G., Ganguly, A., Kwon, M., and Kwasinski, A.; Networking (2018). Performance evaluation of a power-efficient and robust 60 ghz wireless server-to-server datacenter network. IEEE *2*, 1174–1185.

Meijer, A., Berden, G., Arslanov, D., Ozerov, M., Jongma, R., and Van Der Zande, W.J.N.P. (2016). An ultrawide-bandwidth single-sideband modulator for terahertz frequencies. Nat. Photon. *10*, 740–744.

Mendrzik, R., Cabric, D., and Bauch, G. (2018). Error bounds for Terahertz MIMO positioning of swarm UAVs for distributed sensing. IEEE. https://doi.org/10.1109/ICCW.2018.8403688.

Nagatsuma, T., Ducournau, G., and Renaud, C.C.J.N.P. (2016). Advances in terahertz communications accelerated by photonics. Nat. Photon. *10*, 371–379.

Narytnyk, T.J.T., and Engineering, R. (2014). Possibilities of using THz-band radio communication channels for super high-rate backhaul. Telecommun. Radio Eng. *73*, 1361–1371.

Orava, J., Greer, A.L., Gholipour, B., Hewak, D.W., and Smith, C.E. (2012). Characterization of supercooled liquid Ge2Sb2Te5 and its crystallization by ultrafast-heating calorimetry. Nat. Mater. *11*, 279–283.

Peng, B., and Kürner, T. (2015). A stochastic channel model for future wireless THz data centers. IEEE, 741–745. https://doi.org/10.1109/ISWCS.2015.7454448.

Petrov, V., Fodor, G., Kokkoniemi, J., Moltchanov, D., Lehtomaki, J., Andreev, S., Koucheryavy, Y., Juntti, M., and Valkama, M. (2019). On unified vehicular communications and radar sensing in millimeter-wave and low terahertz bands. IEEE Wirel. Commun. *26*, 146–153.

Pirovano, A., Redaelli, A., Pellizzer, F., Ottogalli, F., Tosi, M., Ielmini, D., Lacaita, A.L., and Bez, R. (2004). Reliability study of phase-change nonvolatile memories. IEEE Trans. Device Mater. Reliab. *4*, 422–427.

Pitchappa, P., Kumar, A., Prakash, S., Jani, H., Venkatesan, T., and Singh, R. (2019). Chalcogenide phase change material for active terahertz photonics. Adv. Mater. *31*, 1808157.

Pries, J., Wei, S., Wuttig, M., and Lucas, P. (2019). Switching between crystallization from the glassy and the undercooled liquid phase in phase change material Ge2Sb2Te5. Adv. Mater. *31*, 1900784.

Qu, Y., Li, Q., Du, K., Cai, L., Lu, J., and Qiu, M. (2017). Dynamic thermal emission control based on ultrathin plasmonic metamaterials including phase-changing material GST. Laser Photon. Rev. *11*, 1700091.

Raoux, S., Xiong, F., Wuttig, M., and Pop, E. (2014). Phase change materials and phase change memory. MRS Bull. *39*, 703–710.

Rios, C., Hosseini, P., Wright, C.D., Bhaskaran, H., and Pernice, W.H.P. (2014). On-chip photonic memory elements employing phase-change materials. Adv. Mater. *26*, 1372–1377.

Ríos, C., Stegmaier, M., Hosseini, P., Wang, D., Scherer, T., Wright, C.D., Bhaskaran, H., and Pernice, W.H.P. (2015). Integrated all-photonic non-volatile multi-level memory. Nat. Photon. *9*, 725–732.

Sevison, G.A., Farzinazar, S., Burrow, J.A., Perez, C., Kwon, H., Lee, J., Asheghi, M., Goodson, K.E., Sarangan, A., Hendrickson, J.R., and Agha, I. (2020). Phase change dynamics and two-dimensional 4-bit memory in Ge2Sb2Te5 via telecom-band encoding. ACS Photon. *7*, 480–487.

Shportko, K., Kremers, S., Woda, M., Lencer, D., Robertson, J., and Wuttig, M. (2008). Resonant bonding in crystalline phase-change materials. Nat. Mater. *7*, 653–658.

Siegel, J., Gawelda, W., Puerto, D., Dorronsoro, C., Solis, J., Afonso, C.N., de Sande, J.C.G., Bez, R., Pirovano, A., and Wiemer, C. (2008). Amorphization dynamics of Ge 2 Sb 2 Te 5 films upon nano-and femtosecond laser pulse irradiation. J. Appl. Phys. *103*, 023516.

Simpson, R.E., Fons, P., Kolobov, A.V., Fukaya, T., Krbal, M., Yagi, T., and Tominaga, J. (2011). Interfacial phase-change memory. Nat. Nanotechnol. *6*, 501–505.

Singh, A.K., Singh, S., and Gupta, B.K. (2018). Highly efficient, chemically stable, and UV/blue-light-excitable biluminescent security ink to combat counterfeiting. ACS Appl. Mater. Interfaces *10*, 44570–44575.

Song, H.-J., and Nagatsuma, T. (2011). Present and future of terahertz communications. IEEE Trans. Terahertz Sci. Technol. *1*, 256–263.

Sun, X., Lotnyk, A., Ehrhardt, M., Gerlach, J.W., and Rauschenbach, B. (2017). Realization of multilevel states in phase-change thin films by fast laser pulse irradiation. Adv. Opt. Mater. *5*, 1700169.

Tittl, A., Michel, A.-K.U., Schäferling, M., Yin, X., Gholipour, B., Cui, L., Wuttig, M., Taubner, T., Neubrech, F., and Giessen, H. (2015). A switchable mid-infrared plasmonic perfect absorber with multispectral thermal imaging capability. Adv. Mater. *27*, 4597–4603.

Tonouchi, M. (2007). Cutting-edge terahertz technology. Nat. Photon. *1*, 97–105.

Wang, Q., Rogers, E.T.F., Gholipour, B., Wang, C.-M., Yuan, G., Teng, J., and Zheludev, N.I. (2016). Optically reconfigurable metasurfaces and photonic devices based on phase change materials. Nat. Photon. *10*, 60–65.

Wuttig, M., Bhaskaran, H., and Taubner, T.J.N.P. (2017). Phase-change materials for non-volatile photonic applications. Nat. Photon. *11*, 465–476.

Wuttig, M., Deringer, V.L., Gonze, X., Bichara, C., and Raty, J.Y. (2018). Incipient metals: functional materials with a unique bonding mechanism. Adv. Mater. *30*, 1803777.

Wuttig, M., and Yamada, N. (2007). Phase-change materials for rewriteable data storage. Nat. Mater. *6*, 824–832.

Xiong, L., Liu, B., Liu, D., Lv, L., Hou, Y., Shen, J., and Zhang, B. (2020). An in situ rewritable electrically-erasable photo-memory device for terahertz waves. Nanoscale *12*, 3343–3350.

Yang, K., Hao, Y., Alomainy, A., Abbasi, Q.H., and Qaraqe, K. (2016). Channel modelling of human tissues at terahertz band. IEEE, 218–221. https://doi.org/10.1109/WCNCW.2016.7552702.

Yang, Y., Yamagami, Y., Yu, X., Pitchappa, P., Webber, J., Zhang, B., Fujita, M., Nagatsuma, T., and Singh, R. (2020). Terahertz topological photonics for on-chip communication. Nat. Photon. *14*, 446–451.

Yang, Z., Pan, C., Wang, K., and Shikh-Bahaei, M. (2019). Energy efficient resource allocation in UAV-enabled mobile edge computing networks. IEEE Trans. Wirel. Commun. *18*, 4576–4589.

Zhu, M., Cojocaru-Mirédin, O., Mio, A.M., Keutgen, J., Küpers, M., Yu, Y., Cho, J.Y., Dronskowski, R., and Wuttig, M. (2018). Unique bond breaking in crystalline phase change materials and the quest for metavalent bonding. Adv. Mater. *30*, 1706735.

STAR★METHODS

KEY RESOURCES TABLE

REAGENT or RESOURCE	SOURCE	IDENTIFIER
Chemicals, peptides, and recombinant proteins		
Acetone	Sinopharm	67-64-1
Isopropanol	Sinopharm	67-63-0
Software and algorithms		
OriginPro 2016	Origin Lab	https://originlab.com

RESOURCE AVAILABILITY

Lead contact

Any further information and requests for resources should be directed to and will be fulfilled by the lead contact, Prof. Zhen Tian (tianzhen@tju.edu.cn).

Materials availability

This study did not generate new unique reagents.

Data and code availability

All data reported in this paper will be shared by the lead contact upon request.

This paper does not report original codes.

Any additional information required to reanalyze the data reported in this paper is available from the lead contact upon request.

EXPERIMENTAL MODEL AND SUBJECT DETAILS

Our study does not use experimental models typical in the life sciences.

METHOD DETAILS

Sample fabrication

1 mm-thick high-resistivity silicon (Si) wafers are used as the substrates and cleaned by ultrasonically in acetone, isopropanol, and deionized water in sequence before the deposition. Then, the 80-nm-thick GST film has been deposited on the Si substrate at room temperature by radio frequency (RF) sputtering a GST225 alloy target. The chamber base pressure of 5×10^{-6} mTorr, RF power of 30 W, working pressure of 3 mTorr and gas flow Ar of 13 sccm are employed.

XRD measurements

The size of each sample is 7×7 mm^2, and the sample is irradiated by various laser fluences. Structural analysis of the laser-pumped GST is performed by XRD (Rigaku D/MAX 2500) using Cu Kα radiation, and diffraction patterns are taken in the 2θ range of 20–50° with a scanning step of 0.02°.

THz transmission and imaging measurements

THz transmission of GST samples under various laser fluences is characterized using a homemade terahertz time-domain spectroscopy system (THz-TDS). For THz rewritable multi-level memory, fiber-based terahertz time-domain spectroscopy is employed. The samples are placed on a three-dimensional translation stage, the terahertz waves are focused on the sample through a THz lens, and the transmitted information is collected by a THz receiver. By moving the sample in x- and y-directions, the terahertz transmission of the x-y-plane of the sample can be measured. For high-density photo prints memory, a near-field scanning

terahertz microscopy system that allows 3-D scan of the terahertz electric field is applied. Schematic views of three THz systems are shown in Figure S1.

QUANTIFICATION AND STATISTICAL ANALYSIS

There is no statistical analysis or quantification in this paper.

ADDITIONAL RESOURCES

Any additional information about the film fabrication and tests in this paper is available from the lead contact on request.